Journal of Institute of Science and Technology, 30(2), 01-13 (2025)
ISSN: 2467-9062 (print), e-ISSN: 2467-9240
https://doi.org/10.3126/jist.v30i2.76851

Research Article

FIRST PRINCIPLES STUDY OF THE ELECTRONIC, OPTICAL, ELASTIC, AND THERMAL PROPERTIES OF DOUBLE PEROVSKITE Sr_2MgWO_6 FOR OPTOELECTRONIC APPLICATIONS

Peshal Pokharel [1,2,3], Shashit Kumar Yadav[2*], Devendra Adhikari[2], Nurapati Pantha[1*]
[1]Central Department of Physics, Tribhuvan University, Kritipur, Nepal.
[2]Department of Physics, Mahendra Morang Adarsh Multiple Campus, Tribhuvan University, Biratnagar, Nepal.
[3]Central Campus of Technology, Tribhuvan University, Dharan, Nepal.
**Correspondence: yadavshashit@yahoo.com, mrnurapati@gmail.com*

(Received:** May 31, 2025; **Revised:** October 14, 2025; **Accepted:** October 16, 2025**)

ABSTRACT

The double perovskite Sr_2MgWO_6 exhibits outstanding mechanical, electronic, and optical properties, making it a potential candidate for high-performance optical and optoelectronic applications. In this regard, we investigated the electronic, magnetic, optical, elastic, and structural properties of the double perovskite Sr_2MgWO_6 using the Quantum ESPRESSO code. Structural stability has been confirmed through calculations of formation energy and the tolerance factor. The material exhibited a wide-band-gap (3.18 eV) semiconductor with intense polarization ($\varepsilon_1(\omega) = 12.46$) and a decreasing $\varepsilon_2(\omega)$ peak with photon energy. Elastic parameters, including elastic constants, bulk modulus, shear modulus, and Young's modulus, were determined using the stress-strain method. The calculated elastic constants satisfied Born-Huang criteria for mechanical stability. Calculated high value of bulk modulus (B), and Young's modulus (E) indicated the material's high resistance to volumetric deformation and stiffness, with a moderate shear modulus. A G/B ratio greater than 0.57, a negative Cauchy constant, and a low Poisson's ratio collectively indicated brittle behavior. The calculated Debye temperature of 492.34 K and specific heat capacity (C_v) of 373.4 J/mol-K further emphasized the mechanical strength, thermal stability, and high thermal conductivity of the material. These findings suggest that Sr_2MgWO_6 could be an excellent material for optical waveguides, light-emitting devices, and other optoelectronic technologies.

Keywords: Dielectric, Double perovskite, Electronic properties, Formation energy, Structural stability, Tolerance factor

INTRODUCTION

Perovskite materials have garnered significant attention due to their remarkable structural versatility and wide-ranging applications in photovoltaics (Rahman *et al.*, 2023), thermoelectrics (Aziz *et al.*, 2022), spintronics (Wang *et al.*, 2018), and optoelectronics (Lu *et al.*, 2020). Among these, double perovskites ($A_2BB'O_6$) are particularly noteworthy for their unique structural, electronic, magnetic, and optical properties (Manzoor *et al.*, 2022). The structural flexibility of perovskites enables the incorporation of a diverse array of elements, allowing for the customization of properties tailored to specific technological applications. Recent advances have underscored their potential in renewable energy, data storage, and high-performance electronic systems, establishing them as vital materials in modern materials science (Pokharel *et al.*, 2024a).

Double perovskites were first explored in the early 1950s (Meng *et al.*, 2022) and became widely studied from the late 1950s to the mid-1980s (Tang & Zhu, 2022). Their structure is an extension of simple perovskites, represented by the formula $A_2BB'X_6$. In this structure, A-site cations occupy octahedral positions, B and B' cations are found in tetrahedral and octahedral sites, and X anions fill the spaces between them [Figure 1]. In strontium magnesium tungstate (Sr_2MgWO_6), Sr^{2+} ions occupy the A-site, Mg^{2+}, and W^{6+} ions are situated at the B and B' sites, respectively, and O^{2-} anions are positioned at the X sites. Sr_2MgWO_6, known for its pronounced elastic anisotropy and unique thermal properties, crystallizes in the tetragonal I4/m space group, making it a promising material for further study. Its crystal structure features Sr^{2+} ions coordinated by twelve O^{2-} atoms, forming distorted SrO_{12} cuboctahedra that share corners and faces with adjacent MgO_6 and WO_6 octahedra. The Sr–O bond lengths range from 2.62 Å to 3.01 Å, contributing to the material's elastic and thermal anisotropy. Mg^{2+} ions form MgO_6 octahedra with uniform Mg–O bond lengths of 2.06 Å, while W^{6+} ions are coordinated within WO_6 octahedra, with bond lengths ranging from 1.92 Å to 1.93 Å. These structural characteristics, including corner-sharing

octahedral tilts between 0° and 16°, play a critical role in defining the mechanical stability and electronic properties of Sr_2MgWO_6.

Many double perovskites, particularly those that are environmentally friendly and lead-free, remain underexplored, despite the substantial progress that has been made. These materials provide safer and more sustainable alternatives to the noxious compounds currently used in optoelectronic and thermoelectric applications. Among them, Sr_2MgWO_6 has garnered attention due to its composition of earth-abundant, non-toxic elements. In addition, it has the potential to demonstrate exceptional mechanical stability, a wide band gap, and desirable optical properties.

In this work, we employ density functional theory (DFT) to investigate the ground-state properties of Sr_2MgWO_6, focusing on its elastic anisotropy, thermal stability, and optical characteristics. Our study aims to elucidate the interplay between structural distortions and the material's mechanical and electronic properties under varying pressure conditions. By exploring these properties, we provide new insights into potential applications of the material in thermal management, spintronics, and optoelectronics, contributing to the broader pursuit of eco-friendly, high-performance perovskite materials.

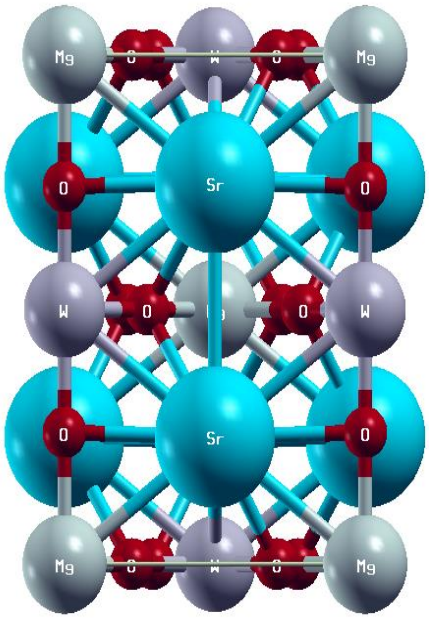

Figure 1. Unit cell of Sr_2MgWO_6 double perovskite.

MATERIALS AND METHODS

The geometrical stability, as well as the elastic and thermal anisotropy of Sr_2ZrMoO_6, was examined through computational methods using the Quantum ESPRESSO code (Giannozzi *et al.*, 2009) based on Density Functional Theory (Koch *et al.*, 2015; Parr *et al.*, 1989) . The spin-polarised electronic band structure of Sr_2MgWO_6 was calculated using both the Generalized Gradient Approximation (GGA) (Langreth & Perdew, 1980; Perdew *et al.*, 1996) and the GGA + U approach (Pokharel *et al.*, 2024). The GGA + U method was applied to account for the on-site Coulomb interactions in the partially filled 5d orbitals of W atoms. Vanderbilt's non-local ultra-soft pseudopotentials (Vanderbilt, 1990) were used for the ion-electron interactions. A plane wave basis set with an energy cutoff of 70 Ry was employed to represent the wave functions precisely. The k-point sampling was carried out with a density of 8 × 8 × 8 for optimization of the structure and the calculation of elastic and thermal properties, a 12 × 12 × 12 grid was employed (Pack & Monkhorst, 1977). The convergence thresholds for total energy and atomic forces were taken at 10^{-6} eV and 10^{-3} eV/Å, respectively. We evaluated the elastic values using the stress-strain approach, which introduced slight deformations in strain and calculated the resulting stress tensors (Golesorkhtabar *et al.*, 2013). The pressure-dependent properties of the material were evaluated by applying isotropic pressure ranging from 0 to 80 GPa. For thermal property calculations, the Debye temperature was estimated using the acoustic velocity derived from the longitudinal and transverse elastic wave velocities (Anderson, 1963). The thermodynamic properties, such as the specific heat capacity (C_V), were calculated using the quasiharmonic Debye model (Blanco *et al.*, 2004).

RESULTS AND DISCUSSION

Structural Properties

In the present calculations, the optimized lattice parameters of the compound are obtained by minimizing the total energy for the unit cell volume. A complete structural optimization is achieved for tetragonal Sr_2MgWO_6 as shown in Figure 2. From the optimized structure, value of lattice parameter is 5.59 Å, and the estimated values of Sr-O, W-O, and Mg-O bond lengths (in Å) were found to be 2.8023, 1.9341, and 2.0698, respectively.

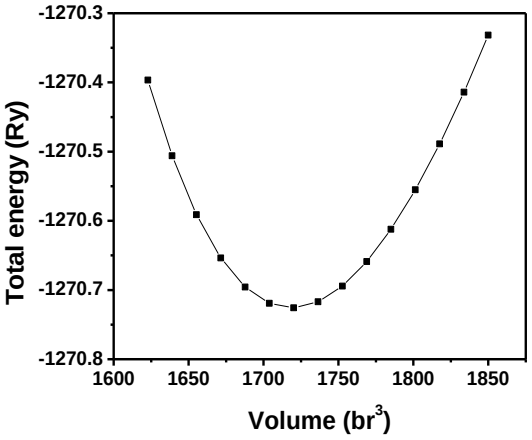

Figure 2. Optimization plots of Sr_2MgWO_6 double perovskite using GGA.

The tolerance factor t helps determine the stable configuration of the material in its ground state (Tidrow, 2014). For a double perovskite material, it is calculated as:

$$t = \frac{r_A + r_O}{\sqrt{2}\,(r_B + r_O)} \qquad (1)$$

Where r_A, r_B, and r_O represent the ionic radii of the Sr cation, the average ionic radius of the Mg and W cations, and the oxygen anion, respectively. The calculated tolerance factor for the material is approximately 0.917, which falls within the stability range of a tetragonal perovskite structure ($0.85 \leq t \leq 0.98$), showing its stability.

Formation energy is an important concept in materials science and solid-state physics, particularly the study of defects, doping, and phase stability. It is defined as the energy required to form a compound, defect, or structure from its constituent elements. The ground state stability has also been evaluated by calculating the formation energy using the following relation (Ray *et al.*, 2021).

$$\Delta H_f = \frac{E_{\text{total}(Sr_2MgWO_6)} - (2E_{Sr} + E_{Mg} + E_W + 6E_O)}{6} \qquad (2)$$

Here, $E_{\text{total}(Sr_2ZrMoO_6)}$ is the equilibrium energy of the Sr_2MgWO_6 perovskite, and E_{Sr}, E_{Mg}, E_W, and E_O are the respective energies of strontium, magnesium, tungsten, and oxygen atoms in their bulk forms. The calculated formation energy for the compound is −7.981 eV/atom. This negative value indicates that the compound is thermodynamically stable, suggesting it is likely to be synthesizable under appropriate experimental conditions (Patwe *et al.*, 2005).

Electronic Properties and Optical Anisotropy

The energy band structure is an important feature for describing the electronic properties of compounds. The electronic states of the transition metal ions are influenced by crystal field splitting and the symmetry of the crystal structure. In this study employs GGA and GGA+U approximations to determine the spin-polarized band structure of double perovskite at high-symmetry k-points. The GGA+U method includes a Hubbard U term, which helps to better represent the localized interactions of electrons in the partially filled 5d orbitals of W (tungsten). This adjustment allows GGA+U to describe the band structure and PDOS of the material more accurately. Using both GGA and GGA + U methods, the calculated band gap of 3.18 eV and also symmetry on the spin-up and spin-down band structure indicate that the non-magnetic nature of the material [Figure 3(a, b)], which matches well with those reported by Dar *et al.* for a wide band gap semiconductor (4.0 eV) double perovskite Ba_2InTaO_6 (Dar *et al.*, 2019).

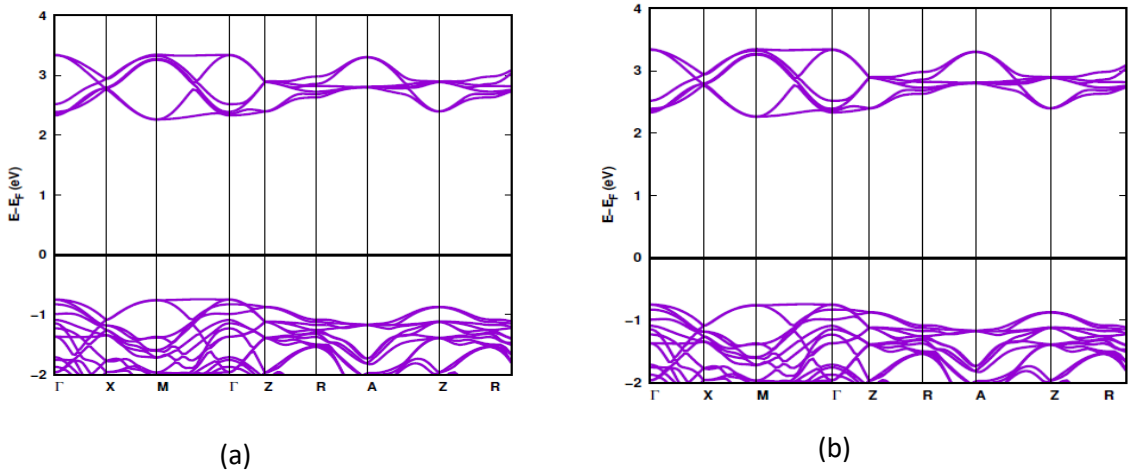

Figure 3. Spin-polarized band structure of Sr_2MgWO_6 double perovskite (a) spin up and (b) spin down within the GGA +U approach.

The PDOS plot [Figure 4] illustrates the contributions of different orbitals (s, p, d) from specific atoms (Sr, Mg, W) to the total density of states (DOS) in the material. The Sr-s and Sr-p orbitals show a relatively minor contribution, while the Mg-d, W-s, and W-d orbitals play a more prominent role, with pronounced peaks indicating a higher density of states at specific energy levels. The substantial contributions of the W-s and W-d orbitals highlight the critical role of tungsten in shaping the electronic properties of the material. The W-d orbitals, in particular, dominate near the Fermi level, making them the primary contributors to the conduction band. Both W-s and W-d orbitals also contribute to the valence band, with W-s orbitals influencing the lower-energy regions and W-d orbitals affecting the higher-energy regions.

The significant presence of W-d orbitals in both the conduction and valence bands suggests that tungsten is a key factor in the material's electrical conductivity. As shown in Figure 4, the observed spin-up/spin-down symmetry confirms the nonmagnetic nature of the perovskite. Its semiconducting character suggests potential for applications in optoelectronic devices such as solar cells.

Optical Properties

Exploring the optical behavior of Sr_2MgWO_6 provides valuable insights into its electronic properties. The interaction of these materials with light provides useful information about their possible applications. Fundamental optical factors like the absorption coefficient, refractive index, and dielectric function are important in determining the feasibility of many optoelectronic devices such as solar cells, LEDs, and lasers. The dielectric function describes the material's optical and electrical properties, including how it interacts with electromagnetic fields at various energy levels. This function is important to understanding how electrons move between energy bands when light is incident on the material.

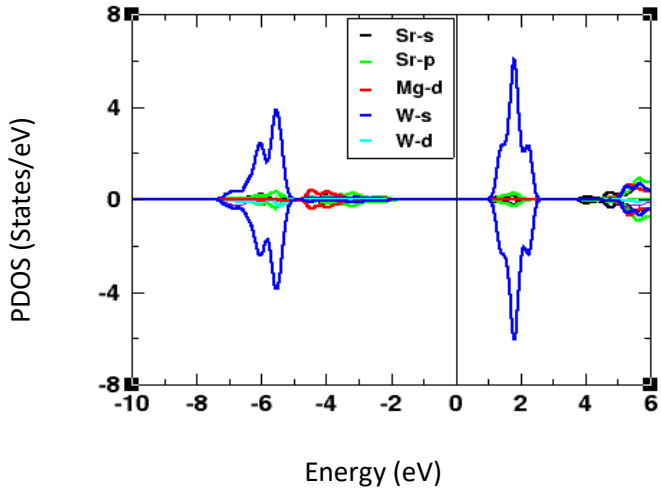

Figure 4. Spin-polarized PDOS plot of Sr_2MgWO_6 double perovskite within the GGA + U approach.

The dispersion relationship of dielectric functions can be determined by examining the connection between the wave vector or leap matrix and the dielectric function (Yang *et al.*, 2022).

The dielectric function is expressed as (Wu *et al.*, 2021):

$$\varepsilon(\omega) = \varepsilon_1(\omega) + i\varepsilon_2(\omega) \qquad (3)$$

And the imaginary component of the dielectric function, $\varepsilon_2(\omega)$, is given as (Lu *et al.*, 2021).

$$\varepsilon_2(\omega) = \frac{8\pi^2 e^2}{2\omega^2 m^2} \sum_n \sum_{n'} \int_{BZ} |P_{nn'}(k)|^2 f_{kn}(1 - f_{kn'})\, \partial(E_n^k - E_{n'}^k - h\omega) \frac{\partial^3 k}{2\pi^3} \qquad (4)$$

Here, f_{kn} is the Fermi-Dirac distribution function, $P_{nn'}(k)$ is the projection of the momentum dipole matrix elements on the direction of the field. $E_n^k(k)$ is the energy of an electron.

An expression derived from the Kramers-Kronig transformation (Lucarini *et al.*, 2005) can be used to compute the real component of the dielectric function, $\varepsilon_1(\omega)$.

$$\varepsilon_1(\omega) = 1 + \frac{2}{\pi} P \int_0^{\infty} \left[\frac{\omega' \varepsilon_2(\omega')}{\omega'^2 - \omega^2}\right] d\omega' \qquad (5)$$

The real part, $\varepsilon_1(\omega)$, describes the ability to disperse and polarize light through the material. On the other

hand, the imaginary part, $\varepsilon_2(\omega)$, indicates the capability to absorb light energy by the material.

These combined optical properties play a crucial role in determining how well the material converts light into energy and its potential for use in high-performance optoelectronic devices.

The other optical parameters, such as absorption coefficient $\alpha(\omega)$, refractive index $n(\omega)$, and reflectivity $R(\omega)$ are expressed in terms of $\varepsilon_1(\omega)$ and $\varepsilon_2(\omega)$ as;

$$\alpha(\omega) = \sqrt{2\omega\sqrt{\{\varepsilon_1(\omega)\}^2 + \{\varepsilon_2(\omega)\}^2} - \varepsilon_1(\omega)} \quad (6)$$

$$n(\omega) = \sqrt{\frac{1}{2}\sqrt{\{\varepsilon_1(\omega)\}^2 + \{\varepsilon_2(\omega)\}^2} + \varepsilon_1(\omega)} \quad (7)$$

$$R(\omega) = \left|\frac{\sqrt{\varepsilon_1(\omega)+i\varepsilon_2(\omega)}-1}{\sqrt{\varepsilon_1(\omega)+i\varepsilon_2(\omega)}+1}\right|^2 \quad (8)$$

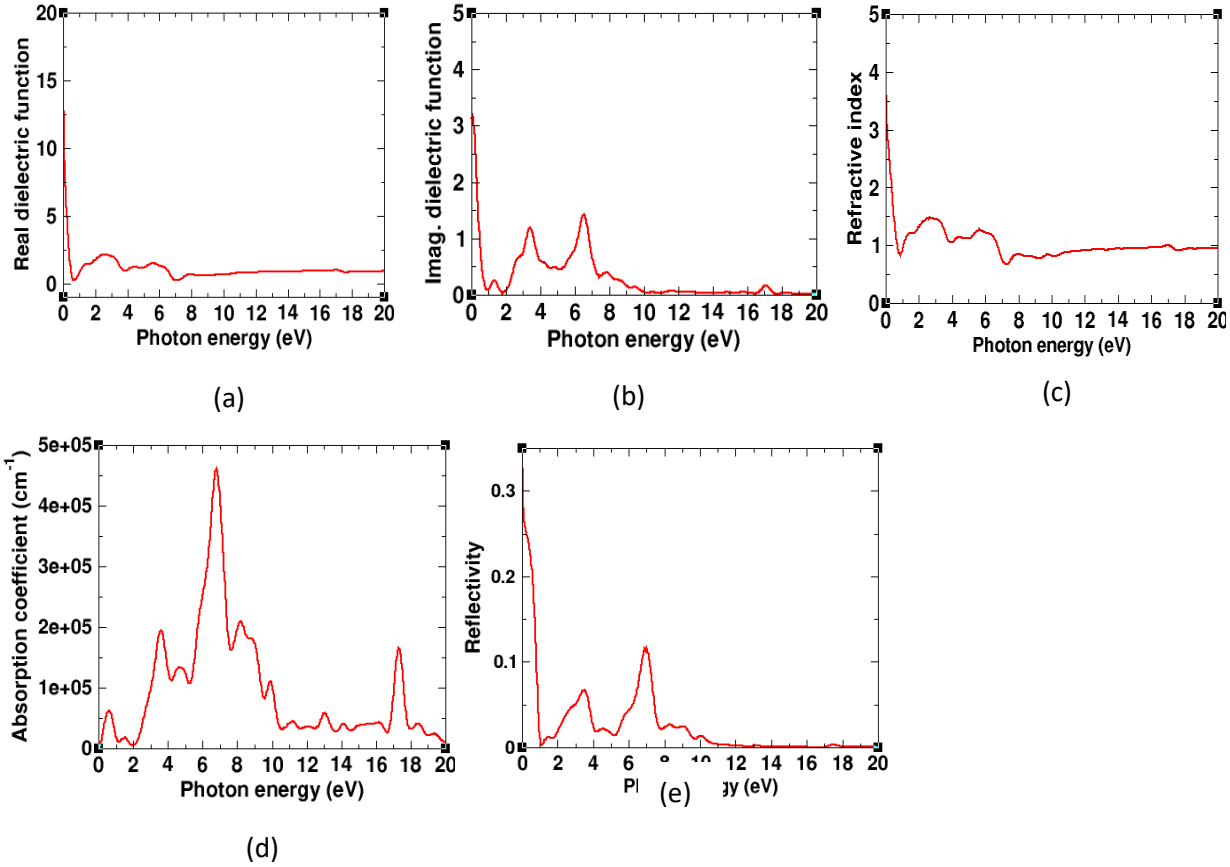

Figure 5. Variation of (a) real and (b) imaginary part of dielectric function (c) refractive index (d) absorption coefficient; (e) reflectivity of Sr_2MgWO_6 double perovskite with photon energy.

Figure 5(a–e) shows the optical parameters that were computed over a photon energy range of 0–20 eV. As shown in Figure 5(a), at static frequency, the polarization response of the material is indicated by the dielectric constant $\varepsilon_1(\omega)$ of 12.46. As photon energy increases, peaks in the dielectric function appear around 2.5 eV, indicating strong interaction with longer wavelengths of light, such as those in the visible or near-infrared regions. The other energy peak at 5.8 eV demonstrates reduced polarizability, corresponding to ultraviolet (UV) light, suggesting potential applications in UV filtering, optoelectronics, and high-frequency devices.

Figure 5(b) illustrates the behavior of $\varepsilon_2(\omega)$ with an initial rise in $\varepsilon_2(\omega)$ which suggests efficient photon absorption at lower energies. This is a result of electronic transitions from the f-orbitals of W or d-orbitals of Mg to unoccupied Sr-3d and O-2p orbitals. The initial increase in $\varepsilon_2(\omega)$ is followed by a decrease, which is a common trend in wide-band-gap semiconductors. These trends emphasize the potential of Sr_2MgWO_6 for optoelectronic applications, where its tunable absorption characteristics could enhance advanced technologies.

Figure 5(c) shows a variation of refractive index, $n(\omega)$ with photon energy. The trend closely follows the real part $\varepsilon_1(\omega)$, highlighting a direct correlation between

the R.I. of material and its polarization response. The R.I. decreases with increasing photon energy, indicating how doping influences the optical characteristics of the material. The absorption coefficient, which is illustrated in Figure 5(d), is a measure that indicates how well a material can absorb light as the energy of the photon increases. It is the interband transitions, which occur when photons with sufficient energy drive electrons to move from the valence band to the conduction band, that are responsible for the significant absorption peak that occurs at approximately 7 eV. This improves the absorption capacity of the material.

Figure 5(e) illustrates the reflectivity spectrum, which offers critical information regarding the light transmission and reflection characteristics of the material. At zero photon energy, the reflectivity is relatively low (0.27), indicating moderate light reflection and suggesting that the material primarily absorbs light at lower energies. As photon energy increases, reflectivity decreases, with distinct peaks at approximately 3.8 eV (0.07) and 6.9 eV (0.12), demonstrating less effective light reflection at higher energies as compared to zero energy. The low reflectivity at lower energies positions the material as a promising candidate for photovoltaic applications, while the peaks at higher energies suggest potential utility in optoelectronic devices.

Elastic Properties

Analysis of the elastic behavior of double perovskite proves essential because it offers fundamental insights into the mechanical stability, dynamic behavior, and strength of materials. This section discusses the mechanical properties and dynamic stability of Sr_2MgWO_6. The tetragonal structure is characterized by six distinct elastic constants (C_{11}, C_{12}, C_{13}, C_{33}, C_{44}, and C_{66}), which were determined using the stress-strain method. These C_{ij} values of Sr_2MgWO_6 are (C_{11} = 228.6 GPa, C_{12} = 69.86 GPa, C_{13} = 101.08 GPa, C_{33} = 229.94, C_{44} =86.96 GPa and C_{66} = 71.58 GPa). The elastic constants provide insight into how a material resists stress from different directions. Specifically, C_{11}, C_{22}, and C_{33} describe how well the material resists deformation along the [100], [010] and [001] directions of the crystal. C_{11} (228.6 GPa) and C_{33} (229.94 GPa) are nearly identical, suggesting that Sr_2MgWO_6 is elastically isotropic along the different directions. The data of C_{44} and C_{66} shows that Sr_2MgWO_6 exhibits moderate shear resistance. The calculated values of C_{ij} that satisfy Born-Huang's mechanical stability criteria (Pokharel *et al.*, 2025) for a tetragonal system

$C_{11} > 0$, $C_{33} > 0$, $C_{44} > 0$, $C_{66} > 0$, $C_{11}–C_{12} > 0$,

$C_{11}+ C_{33}– 2C_{13} > 0$, $2C_{11}+2C_{12}+ C_{33} + 4C_{13} > 0$ (9)

Hooke's law (Bao *et al.*, 2020) describes the dependence of stress (σ_{ij}) to strain (ε_{kl}) in terms of C_{ij} as follows

$$\sigma_{ij} = C_{ijkl}\varepsilon_{kl} \Rightarrow \sigma_{ij} = C_{ij}\varepsilon_{ij} \quad (10)$$

where σ_{ij} is the stress tensor, C_{ij} is the stiffness tensor and ε_{ij} is the strain component.

The Voigt-Reuss-Hill method (Voigt, 1928) (Reuss, 1929) (Hill, 1952) can be used to determine the values of B and G for the tetragonal system and are given as

$$B_V = \frac{1}{9}[2C_{11} + C_{33} + 2C_{12} + 4C_{13}] \quad 11(a)$$

$$B_R = \frac{C^2}{M} \quad 11(b)$$

the shear constant (G_v) of an upper limit is

$$G_V = \frac{1}{30}[M + 3C_{11} - 3C_{12} + 12C_{44} + 6C_{66}] \quad 11(c)$$

with $M = [C_{11} + C_{12} + 2C_{33} - 4C_{44}]$

and $C^2 = (C_{11} + C_{12})C_{33} - 2{C_{13}}^2$

and its lower limit can be expressed in the form as

$$G_R = \frac{15}{[\frac{18B_V}{C^2} + \frac{6}{C_{11}+C_{12}} + \frac{6}{C_{44}} + \frac{3}{C_{66}}]} \quad 11(d)$$

Finally, Voigt and Reuss's mean values are obtained by

$B_H = \frac{(B_V+B_R)}{2}$ and $G_H = \frac{(G_V+G_R)}{2}$

$$E = \frac{9B_HG_H}{3B_H+G_H} \quad 11(e)$$

$$v = \frac{3B_H-2G_H}{2(3B_H+G_H)} \quad 11(f)$$

$$P_C = C_{13}- C_{44} \quad 11(g)$$

The elastic constants listed above were utilized to calculate additional mechanical parameters, including the bulk modulus (B), Young's modulus (Y), and shear modulus (G), using equations 11(a-g). The computed values, such as elastic moduli (E, B, G), Poisson's ratio (ν), and Pugh's ratio (G/B), for the Sr_2MgWO_6 double perovskite, are displayed in Table 1. The high bulk modulus value implies good resistance to volumetric deformation and indicates the material is relatively incompressible. The moderate shear modulus suggests that the compound has a balance between rigidity and flexibility. Furthermore, the high Y values indicate the stiffness of the material, illustrating its strong mechanical abilities as a double perovskite.

Table 1. Calculated values of elastic moduli (B, G, E), Poisson's ratio (υ), G_H/B_H ratio of Sr_2MgWO_6 double perovskites.

B_V (GPa)	B_R (GPa)	B_H (GPa)	G_V (GPa)	G_R (GPa)	G_H (GPa)	E (GPa)	υ	G_H/B_H
129.84	129.39	129.61	78.84	77.60	78.22	195.36	0.249	0.603

The tabulated values of elastic moduli (E, B, G), and the elastic constants (C_{ij}) described above, demonstrate patterns that follow the common behavior noticed in half-metallic double perovskite oxide Sr_2MnTaO_6, as reported by Dar *et al.* (2019) in their study (Dar *et al.*, 2019).

The G/B ratio is a critical parameter for evaluating whether materials exhibit ductile or brittle behavior (Thompson & Clegg, 2018). The materials with $\frac{G}{B} > 0.57$ are considered brittle, while those with $\frac{G}{B} < 0.57$ are classified as ductile. For the material under study, the calculated G/B ratio consistently exceeds 0.57. This indicates that the material retains brittle behavior even under high pressure. Additionally, the negative Cauchy constant further supports the brittle nature of the material.

Elastic Anisotropy

Anisotropy indexes are useful for assessing the mechanical, thermal, and electrical characteristics of a material. The universal anisotropy index (A^U) provides a thorough evaluation of overall anisotropy (Ranganathan & Ostoja-Starzewski, 2008). Furthermore, the shear anisotropy indexes (A_{shear}) and bulk anisotropy (A_{comp}) offer important information about how the material behaves under shear strains and compression, respectively (Miao *et al.*, 2011). These parameters are important for the analysis of the elastic anisotropy of double perovskites under isotropic pressure (Nye, 1985). These indices are defined as follows.

$$A^U = 5\frac{B_V}{B_R} + \frac{G_V}{G_R}6 \qquad 12(a)$$

$$A^Z = \frac{2C_{44}}{C_{11}-C_{12}} \qquad 12(b)$$

$$A_{comp} = \frac{B_V-B_R}{B_V+B_R} \qquad 12(c)$$

$$A_{shear} = \frac{G_V-G_R}{G_V+G_R} \qquad 12(d)$$

Isotropic behavior is indicated when A^U, A_{comp}, and A_{shear} are all equal to 0, while any non-zero values indicate the presence of anisotropy. Moreover, the degree of anisotropy rises as the values of A^U, A_{comp}, and A_{shear} are increased. The compound exhibits an isotropic bulk modulus as indicated A_{comp} = 0. However, the non-zero values of A^U and A_{shear} in Table 2 suggest that the shear modulus and Young's modulus vary across different crystallographic directions, indicating elastic anisotropy in shear and stiffness. In a tetragonal crystal, the anisotropy factors $A_{\{100\}}$, $A_{\{010\}}$ and $A_{\{010\}}$ are defines as (Zhai *et al.*, 2012):

$$A_1 = A_{\{100\}} = \frac{4C_{44}}{C_{11}+C_{33}-2C_{13}} \qquad 13(a)$$

$$A_2 = A_{\{010\}} = \frac{4C_{55}}{C_{22}+C_{33}-2C_{23}} \qquad 13(b)$$

$$A_3 = A_{\{010\}} = \frac{2C_{66}}{C_{11}-C_{12}} \qquad 13(c)$$

These equations further illustrate the anisotropic nature of the shear modulus in different crystallographic directions.

Table 2. Calculated elastic anisotropy indexes ($A^U, A^Z, A_{comp}, A_{shear}, A_1, A_2, A_3$) of the Sr_2MgWO_6 double perovskites.

A^U	A_{comp}	A_{shear}	A_1	A_2	A_3
1.0956	0.00173	0.0079	1.357	1.357	0.902

As reported in Table 2, the calculated values of A^U, A_1 and A_2 are greater than 1, while that of A_3 is less than 1. They collectively indicate a significant deviation from isotropic behaviour. To further illustrate this anisotropy, 2D polar plots of B, G, and ν were constructed, which offer a more precise visualization of their directional dependence across different crystallographic planes. These parameters are expressed in terms of the elastic compliance constants (S_{ij}) and directional cosines (l_i) (Pokharel *et al.*, 2024b).

$$\frac{1}{E} = S_{11}(l_1^4 + l_2^4) + (2.S_{13} + S_{44})(l_2^2.l_3^2 + l_1^2.l_3^2) + S_{33}.l_3^4 + (2.S_{12} + S_{66})\, l_1^2.l_2^2. \quad 14(a)$$

$$\frac{1}{B} = (S_{11} + S_{12} + S_{13}) - (S_{11} + S_{12} - S_{13} - S_{33}).l_3^2 \quad 14(b)$$

$$\frac{1}{G} = \frac{1}{2}(S_{44} + S_{66})(l_1^4 + l_2^4) + S_{44}l_3^4 + l_1^2.l_2^2[4(S_{11} - S_{12}) + (S_{44} - S_{66})] + l_3^2(1 - l_3^2)\left[2(S_{11} + S_{12} - 2S_{13}) + \frac{1}{2}(S_{66} - S_{44})\right]. \quad 14(c)$$

$$\text{and } (\Theta) = \frac{[\,C_{12}cos^4(\Theta) - Bcos^2(\Theta)sin^2(\Theta) + C_{12}sin^4(\Theta)\,]}{[\,C_{22}cos^4(\Theta) + Acos^2(\Theta)sin^2(\Theta) + C_{11}sin^4(\Theta)\,]} \quad 14(d)$$

$$\text{where, } A = \frac{(C_{11}C_{22} - C_{12}^2)}{C_{66}} - 2C_{11} \text{ and } B = C_{11} + C_{22} - \frac{(C_{11}C_{22} - C_{12}^2)}{C_{66}}. \quad 14(e)$$

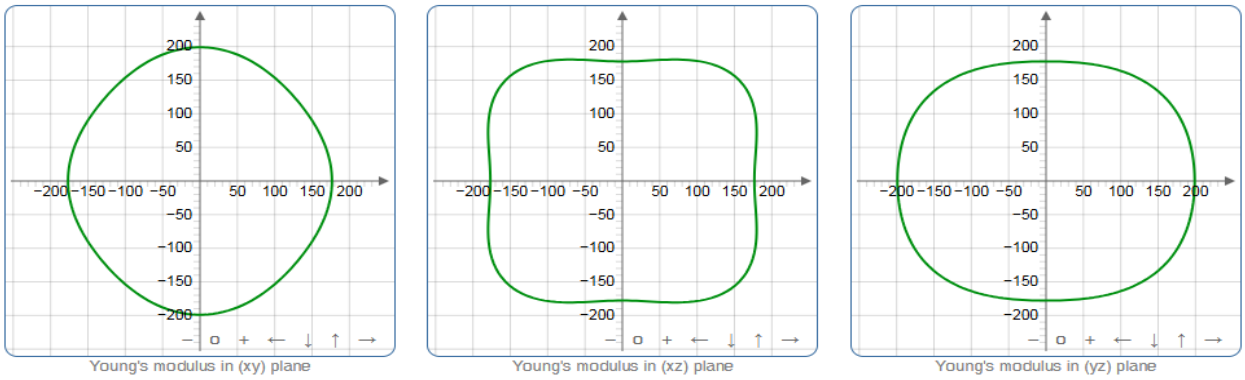

Figure 6: Polar plots of the variation of Young's modulus of Sr_2MgWO_6.

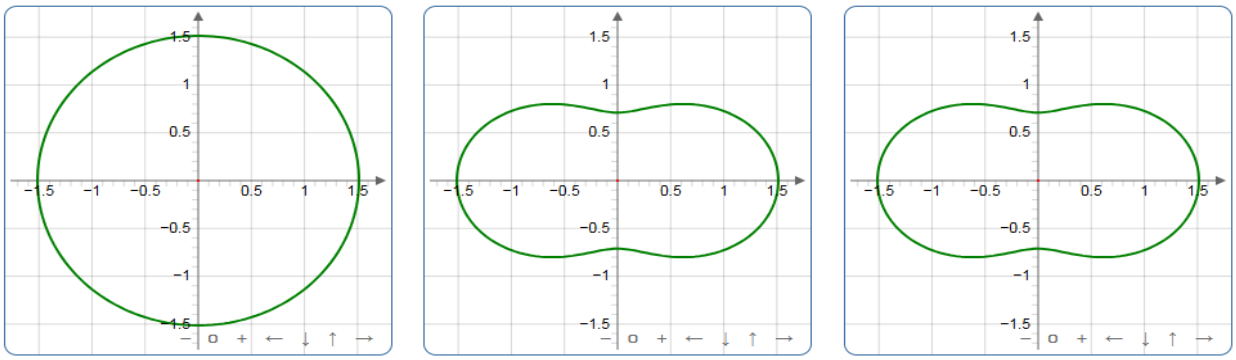

Figure 7. Polar plots of the variation of bulk modulus of Sr_2MgWO_6.

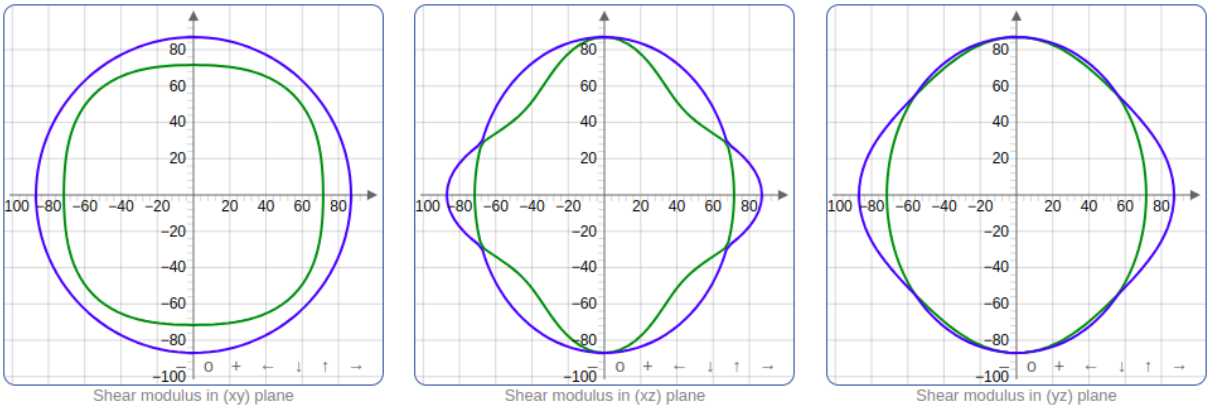

Figure 8. Polar plots of the variation of the shear modulus of Sr_2MgWO_6.

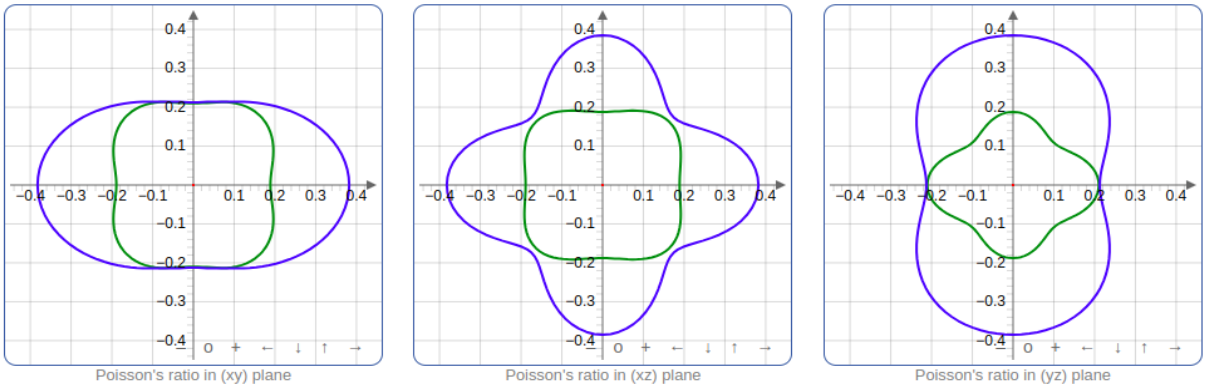

Figure 9. Polar plots of the variation of Poisson's ratio of Sr_2MgWO_6.

Figures 6, 7, 8, and 9 present polar plots illustrating the variation of E, B, G, and Poisson's ratio for Sr_2MgWO_6. These plots reveal a strong directional dependence of the elastic moduli, indicating that their values vary with specific crystallographic orientations within the material. The nearly circular plot of Young's modulus in the xy plane suggests an almost isotropic response, indicating the material offers uniform resistance to deformation in all directions within this plane. However, the elliptical plots in the xz and yz planes reflect anisotropic behavior. This anisotropic behavior shows that Young's modulus changes with the orientation of the applied stress in these planes [Figure 6]. The circular plot of bulk modulus in the xy plane indicates an almost isotropic volumetric response, suggesting that the material exhibits uniform resistance to compression in all directions within this plane. In contrast, the elliptical shapes observed in the xz and yz planes reflect anisotropic compressibility, showing that the bulk modulus varies with the direction of applied stress [Figure 7]. The shear modulus polar plot in the xy plane exhibits a nearly circular shape, indicating isotropic shear behavior within this plane. This reflects a uniform resistance to shear deformation in all directions of the xy plane. In contrast, the elliptical contours observed in the xz and yz planes reveal anisotropic shear behavior [Figure 8], with the resistance to shear deformation varying with direction. Figure 9 shows the directional variation of Poisson's ratio, with non-circular contour shapes indicating that the material is not perfectly isotropic. Overall, these findings reveal that the mechanical properties of Sr_2MgWO_6 are highly sensitive to crystallographic direction.

Debye Temperature

The Debye temperature (θ_D) is a key temperature that represents the vibrational characteristics of a solid. Above the θ_D all vibrational modes are active; below which quantum effects play a significant role. The expression of Debye temperature is established from acoustic velocities and elastic constant data (Anderson, 1963; Pokharel *et al.*, 2024b). The equation below accurately estimates the θ_D value based on the average sound velocity (v_m).

$$\theta_D = \frac{h}{K_B}\left[\frac{3n}{4\pi}\left(\frac{N_A.\rho}{M}\right)\right]^{\frac{1}{3}} v_m \qquad (15)$$

Where h is Planck's constant, K_B is Boltzmann's constant, n is the number of atoms in each formula unit, N_A is Avogadro's number, M is the molecular weight, ρ is density, and v_m is the average sound velocity. The average sound velocity is given by (Wu *et al.*, 2020)

$$v_m = \left[\frac{1}{3}\left(\frac{2}{v_t^3} + \frac{1}{v_l^3}\right)\right]^{\frac{-1}{3}} \qquad (16)$$

Here, v_l and v_t represent the velocities of longitudinal and transverse elastic waves, respectively, and can be obtained from Navier's equation (Bao *et al.*, 2019)

$$v_l = \left[\frac{3B+4G}{3\rho}\right]^{\frac{1}{2}}, \text{ and } v_t = \left[\frac{G}{\rho}\right]^{\frac{1}{2}} \qquad (17)$$

The longitudinal velocity v_l, transverse velocity v_t, and average sound velocity v_m are determined to be 6145.95 m s^{-1}, 3466.32 ms^{-1}, and 3844.87 ms^{-1}, respectively.

The longitudinal velocity is significantly greater than the transverse velocity, which highlights the material's inherent anisotropy in wave propagation between compressive and shear modes. The Debye temperature θ_D is 492.34 K. Overall, the high sound velocities and Debye temperature indicate that the material exhibits excellent mechanical strength, thermal resistance, and potentially high thermal conductivity, making it a promising candidate for applications in high-performance electronics and thermal management technologies.

Thermodynamic Properties

The thermodynamic properties, including the specific heat capacity (C_V), were calculated using the quasiharmonic Debye model (Blanco *et al.*, 2004) across a temperature range of 0 - 800 K. These computations were performed based on the equation of state-derived from the quasiharmonic approximation of the Debye model. The specific heat capacity is given by the following expression:

$$C_V = 3nK[4\mathrm{D}(\theta/\mathrm{T})\left(\frac{\theta_D}{T}\right) - \frac{\frac{3\theta_D}{T}}{e^{\frac{\theta_D}{T}}-1}] \qquad (18)$$

Where n represents the number of atoms per formula unit, K is Boltzmann constant, θ_D the Debye temperature, and D(θ/T) is the Debye integral and is defined as

$$\mathrm{D}(\theta/\mathrm{T}) = \frac{3}{\left(\frac{\theta}{T}\right)^3}\int_0^{\theta/\mathrm{T}} \frac{x^3}{e^x-1}\,dx \qquad (19)$$

Figure 10 presents the variation of specific heat (C_V), as a function of temperature (0–800 K) at constant volume for Sr_2MgWO_6 perovskite. The specific heat at constant volume represents the material's ability to store thermal energy via vibrational modes in the crystal lattice. At low temperatures (< 300 K), C_V increases rapidly with temperature. The gradual increase in vibrational modes is responsible for this behavior, as thermal energy becomes sufficient to excite lower-frequency phonons. At higher temperatures (> 300 K), C_V approaches a plateau near the Dulong-Petit limit. The specific heat C_V from equation 15 is found to be 373.42 J/(mol·K).

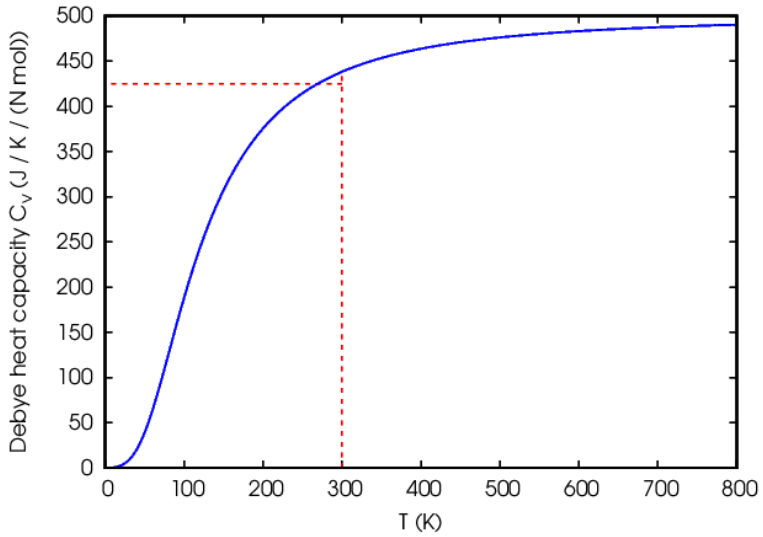

Figure 10. Variation of specific heat capacity of Sr_2MgWO_6 double perovskite with temperature.

CONCLUSIONS

This study demonstrates that the double perovskite Sr_2MgWO_6 possesses significant elastic, thermal, and optical anisotropy. This material exhibits strong resistance to uniaxial compression, particularly along the [001] direction, indicating strong atomic bonding along this axis. The rise in bulk, shear, and Young's moduli indicates enhanced mechanical stability of the material. However, the high G/B ratio, negative Cauchy constant, and low Poisson's ratio indicate that Sr_2MgWO_6 remains brittle under compression, characterized by strong covalent bonding.

Thermal conductivity of the material is direction-dependent, reflecting anisotropic phonon transport. The minimum thermal conductivity ($k_{\min}$) varies with pressure and crystallographic direction, following the order [001] > [110] > [100], suggesting more efficient acoustic transport along [001] and increased phonon scattering along [110] and [100]. The high Debye temperature (θ_D) = 492.34 K) supports the material's strong interatomic forces and thermal stability. Additionally, the specific heat capacity (C_V) increases rapidly below 300 K due to low-frequency phonon excitation and saturates at higher temperatures, reaching a value of 373.42 J/mol·K. These findings highlight Sr_2MgWO_6 as a mechanically stable, thermally resistant, and directionally anisotropic material, making it a promising candidate for applications in thermal management and high-performance electronic devices.

ACKNOWLEDGEMENTS

The authors are grateful to the Department of Physics, Mahendra Morang Adarsh Multiple Campus, Tribhuvan University, Biratnagar, Nepal, for providing computational facilities.

AUTHOR CONTRIBUTIONS

Conceptualization: PP; Investigation: KKB, DNC; Methodology: PP, SKY; Data curation: DA; Data analysis: NP, DA; Writing - original draft: PP, SKY; Writing - review and editing: DA, NP, SKY.

CONFLICT OF INTEREST

The authors declare that they have no known competing financial interests or personal relationships that could have appeared to influence the work reported in this paper.

DATA AVAILABILITY STATEMENT

The data of the present work will be made available by the corresponding authors upon request.

REFERENCES

Anderson, O. L. (1963). A simplified method for calculating the Debye temperature from elastic constants. *Journal of Physics and Chemistry of Solids*, *24*(7), 909–917. https://doi.org/10.1016/0022-3697(63)90067-2.

Aziz, A., Aldaghfag, S. A., Zahid, M., Iqbal, J., Yaseen, M., & Somaily, H. H. (2022). Theoretical investigation of X_2NaIO_6 (X= Pb, Sr) double perovskites for thermoelectric and optoelectronic applications. *Physica B: Condensed Matter*, *630*, 413694. https://doi.org/10.1016/j.physb.2022.413694.

Bao, L., Kong, Z., Qu, D., & Duan, Y. (2020). Revealing the elastic properties and anisotropies of Mg_2X (X = Si, Ge and Sn) with different structures from a first-principles calculation. *Materials Today Communications*, *24*, 101337. https://doi.org/10.1016/j.mtcomm.2020.101337.

Bao, W., Liu, D., Li, P., & Duan, Y. (2019). Structural properties, elastic anisotropies and thermal conductivities of tetragonal LnB_2C_2 (Ln = Rare Earth) compounds from first-principles calculations. *Ceramics International*, *45*(2), 1857–1867. https://doi.org/10.1016/j.ceramint.2018.10.077.

Blanco, M. A., Francisco, E., & Luaña, V. (2004). GIBBS: Isothermal-isobaric thermodynamics of solids from energy curves using a quasi-harmonic Debye model. *Computer Physics Communications*, *158(1)*, 57–72. https://doi.org/10.1016/j.comphy.2003.12.001.

Dar, S. A., Sharma, R., Srivastava, V., & Sakalle, U. K. (2019). Investigation on the electronic structure, optical, elastic, mechanical, thermodynamic and thermoelectric properties of wide band gap semiconductor double perovskite Ba_2InTaO_6. *RSC Advances*, *9*(17), 9522–9532. https://doi.org/10.1039/C9RA00313D.

Dar, S. A., Srivastava, V., & Sakalle, U. K. (2019). Structural, elastic, mechanical, electronic, magnetic, thermoelectric and thermodynamic investigation of half-metallic double perovskite oxide Sr_2MnTaO_6. *Journal of Magnetism and Magnetic Materials*, *484*, 298–306. https://doi.org/10.1016/j.jmmm.2019.04.048.

Giannozzi, P., Baroni, S., Bonini, N., Calandra, M., Car, R., Cavazzoni, C., Ceresoli, D., Chiarotti, G. L., Cococcioni, M., Dabo, I., Dal Corso, A., de Gironcoli, S., Fabris, S., Fratesi, G., Gebauer, R., Gerstmann, U., Gougoussis, C., Kokalj, A., Lazzeri, M., Wentzcovitch, R. M. (2009). QUANTUM ESPRESSO: A modular and open-

source software project for quantum simulations of materials. *Journal of Physics: Condensed Matter*, *21(*39*)*, 395502. https://doi.org/10.1088/0953-8984/21/39/395502.

Golesorkhtabar, R., Pavone, P., Spitaler, J., Puschnig, P., & Draxl, C. (2013). Elastic: A tool for calculating second-order elastic constants from first principles. *Computer Physics Communications*, *184*(8), 1861–1873. https://doi.org/10.1016/j.cpc.2013.03.010.

Hill, R. (1952). The Elastic Behaviour of a Crystalline Aggregate. *Proceedings of the Physical Society. Section A*, *65*(5), 349–354. https://doi.org/10.1088/0370-1298/65/5/307.

Nye, J. F. (1985). *Physical properties of crystals: Their representation by tensors and matrices*. Oxford university press.

Koch, W., & Holthausen, M. C. (2015). *A chemist's guide to density functional theory*. John Wiley & Sons.

Lucarini, V., Peiponen, K. E., Saarinen, J. J., & Vartiainen, E. M. (2005). Kramers-Kronig relations in optical materials research. Berlin, Heidelberg: Springer Berlin Heidelberg.

Langreth, D. C., & Perdew, J. P. (1980). Theory of nonuniform electronic systems. I. Analysis of the gradient approximation and a generalization that works. *Physical Review B*, *21*(12), 5469–5493. https://doi.org/10.1103/PhysRevB.21.5469.

Lu, L., Pan, X., Luo, J., & Sun, Z. (2020). Recent Advances and Optoelectronic Applications of Lead-Free Halide Double Perovskites. *Chemistry – A European Journal*, *26*(71), 16975–16984. https://doi.org/10.1002/chem.202000788.

Lu, Y., Duan, Y., Peng, M., Yi, J., & Li, C. (2021). First-principles calculations of electronic, optical, phononic and thermodynamic properties of C40-type $TMSi_2$ (TM = Cr, Mo, W) disilicides. *Vacuum*, *191*, 110324. https://doi.org/10.1016/j.vacuum.2021.110324.

Manzoor, M., Bahera, D., Sharma, R., Tufail, F., Iqbal, M. W., & Mukherjee, S. K. (2022). Investigated the structural, optoelectronic, mechanical, and thermoelectric properties of Sr_2BTaO_6 (B = Sb, Bi) for solar cell applications. *International Journal of Energy Research*, *46*(15), 23698–23714. https://doi.org/10.1002/er.8669.

Meng, Y., Li, X., Wang, S., Lau, C., Hu, H., Ke, Y., Tan, G., Yang, J., & Long, Y. (2022). Flexible smart photovoltaic foil for energy generation and conservation in buildings. *Nano Energy*, *91*, 106632. https://doi.org/10.1016/j.nanoen.2021.106632.

Miao, N., Sa, B., Zhou, J., & Sun, Z. (2011). Theoretical investigation on the transition-metal borides with Ta_3B_4-type structure: A class of hard and refractory materials. *Computational Materials Science*, *50*(4), 1559–1566. https://doi.org/10.1016/j.commatsci.2010.12.015.

Pack, J. D., & Monkhorst, H. J. (1977). Special points for Brillouin-zone integrations—a reply. *Physical Review B*, *16*(4), 1748–1749. https://doi.org/10.1103/PhysRevB.16.1748.

Parr, R. G., & Yang, W. (1989). *Density functional theory of atoms and molecules* (2nd ed.). Oxford University Press.

Patwe, S. J., Achary, S. N., Mathews, M. D., & Tyagi, A. K. (2005). Synthesis, phase transition and thermal expansion studies on M_2MgWO_6 ($M=Ba^{2+}$ and Sr^{2+}) double perovskites. *Journal of Alloys and Compounds*, *390*(1–2), 100–105. https://doi.org/10.1016/j.jallcom.2004.05.093.

Perdew, J. P., Burke, K., & Ernzerhof, M. (1996). Generalized Gradient Approximation Made Simple. *Physical Review Letters*, *77*(18), 3865–3868. https://doi.org/10.1103/PhysRevLett.77.3865.

Pokharel, P., Yadav, S. K., Pantha, N., & Adhikari, D. (2024a). First-Principles Investigations of Structural, Electronic, and Elastic Properties of $ZrSiO_3$ Perovskite: Layer Dependence, Surface Termination, and Pressure Effects. *Physica Status Solidi (b)*, *261*(8) 2400156. https://doi.org/10.1002/pssb.202400156.

Pokharel, P., Yadav, S. K., Pantha, N., & Adhikari, D. (2024b). Strain-dependent electronic, mechanical and piezoelectric properties of $ZrSiO_3$ 2D monolayer: A first principles approach. *Journal of Physics and Chemistry of Solids*, *193*, 112198. https://doi.org/10.1016/j.jpcs.2024.112198.

Pokharel, P., Yadav, S. K., Pantha, N., Sharma, B., & Adhikari, D. (2024). Structural, electronic, optical, magnetic, and mechanical properties of $SmMnO_3$ perovskite with europium and yttrium doping: A first-principles study. *AIP Advances*, *14*(12), 125309 https://doi.org/10.1063/5.0232439.

Pokharel, P., Yadav, S. K., Pantha, N., Sharma, B., & Adhikari, D. (2025). Elastic Anisotropy and Thermal Properties of Sr_2ZrMoO_6 Double Perovskite under Different Pressures. *Physica Status Solidi (b)*, 262(5), 2400625. https://doi.org/10.1002/pssb.202400625.

Rahman, Md. A., Hasan, W., Hasan, Md. Z., Irfan, A., Mouna, S. C., Rukaia khatun, Razzaque Sarker, Md. A., Rahaman, Md. Z., & Rahman, M. (2023). Structural, mechanical, electronic, optical and thermodynamic features of lead-free oxide perovskites $AMnO_3$ (A=Ca, Sr, Ba): DFT simulation based comparative study. *Physica B:*

Condensed Matter, *668*, 415215. https://doi.org/10.1016/j.physb.2023.415215.

Ranganathan, S. I., & Ostoja-Starzewski, M. (2008). Universal Elastic Anisotropy Index. *Physical Review Letters*, *101*(5), 055504. https://doi.org/10.1103/PhysRevLett.101.055504.

Ray, R. B., Kaphle, G. C., Rai, R. K., Yadav, D. K., Paudel, R., & Paudyal, D. (2021). Strain induced electronic structure, and magnetic and structural properties in quaternary Heusler alloys ZrRhTiZ (Z = Al, In). *Journal of Alloys and Compounds*, *867*, 158906. https://doi.org/10.1016/j.jallcom.2021.158906.

Reuss, A. (1929). Berechnung der Fließgrenze von Mischkristallen auf Grund der Plastizitätsbedingung für Einkristalle . *ZAMM - Journal of Applied Mathematics and Mechanics / Zeitschrift Für Angewandte Mathematik Und Mechanik*, *9*(1), 49–58. https://doi.org/10.1002/zamm.19290090104.

Tang, Q., & Zhu, X. (2022). Half-metallic double perovskite oxides: recent developments and future perspectives. *Journal of Materials Chemistry C*, *10*(41), 15301–15338. https://doi.org/10.1039/D2TC03199J

Thompson, R. P., & Clegg, W. J. (2018). Predicting whether a material is ductile or brittle. *Current Opinion in Solid State and Materials Science*, *22*(3), 100–108. https://doi.org/10.1016/j.cossms.2018.04.001

Tidrow, S. C. (2014). Mapping Comparison of Goldschmidt's Tolerance Factor with Perovskite Structural Conditions. *Ferroelectrics*, *470*(1), 13–27. https://doi.org/10.1080/00150193.2014.922372.

Vanderbilt, D. (1990). Soft self-consistent pseudopotentials in a generalized eigenvalue formalism. *Physical Review B*, *41*(11), 7892–7895. https://doi.org/10.1103/PhysRevB.41.7892.

Wang, Y., Lv, Z., Zhou, L., Chen, X., Chen, J., Zhou, Y., Roy, V. A. L., & Han, S.-T. (2018). Emerging perovskite materials for high density data storage and artificial synapses. *Journal of Materials Chemistry C*, *6*(7), 1600–1617. https://doi.org/10.1039/C7TC05326F.

Wu, Y., Bao, L., Wang, X., Wang, Y., Peng, M., & Duan, Y. (2020). Insight into structural, electronic, elastic and thermal properties of A15-type Nb_3X (X = Si, Ge, Sn and Pb) compounds. *Materials Today Communications*, *25*, 101410. https://doi.org/10.1016/j.mtcomm.2020.101410.

Wu, Y., Wang, X., Wang, Y., Duan, Y., & Peng, M. (2021). Insights into electronic and optical properties of $AGdS_2$ (A = Li, Na, K, Rb and Cs) ternary gadolinium sulfides. *Optical Materials*, *114*, 110963. https://doi.org/10.1016/j.optmat.2021.110963.

Voigt, W. (1928). *A determination of the elastic constants for beta-quartz*, Lehrbuch der Kristallphysik. Terubner Leipzig, 40, 2856-2860.

Yang, C., Wu, Y., & Duan, Y. (2022). Theoretical predictions of the electronic, optical and thermodynamic properties of the C40-type $TMSi_2$ (TM = V, Nb and Ta) disilicides. *Materials Today Communications*, *30*, 103115. https://doi.org/10.1016/j.mtcomm.2021.103115.

Zhai, H., Li, X., & Du, J. (2012). First-Principles Calculations on Elasticity and Anisotropy of Tetragonal Tungsten Dinitride under Pressure. *Materials Transactions*, *53*(7), 1247–1251. https://doi.org/10.2320/matertrans.M2011373.